Cathodic Electrodeposition of Ni—Mo on Semiconducting NiFe$_2$O$_4$ for Photoelectrochemical Hydrogen Evolution in Alkaline Media

Jochem H. J. Wijten,[a] Ronald P. H. Jong,[b] Guido Mul,[b] and Bert M. Weckhuysen*[a]

Photocathodes for hydrogen evolution from water were made by electrodeposition of Ni—Mo layers on NiFe$_2$O$_4$ substrates, deposited by spin coating on F:SnO$_2$-glass. Analysis confirmed the formation of two separate layers, without significant reduction of NiFe$_2$O$_4$. Bare NiFe$_2$O$_4$ was found to be unstable under alkaline conditions during (photo)electrochemistry. To improve the stability significantly, the deposition of a bifunctional Ni—Mo layer through a facile electrodeposition process was performed and the composite electrodes showed stable operation for at least 1 h. Moreover, photocurrents up to -2.1 mA cm^{-2} at -0.3 V vs. RHE were obtained for Ni—Mo/NiFe$_2$O$_4$ under ambient conditions, showing that the new combination functions as both a stabilizing and catalytic layer for the photoelectrochemical evolution of hydrogen. The photoelectrochemical response of these composite electrodes decreased with increasing NiFe$_2$O$_4$ layer thickness. Transient absorption spectroscopy showed that the lifetime of excited states is short and on the ns timescale. An increase in lifetime was observed for NiFe$_2$O$_4$ of large layer thickness, likely explained by decreasing the defect density in the primary layer(s), as a result of repetitive annealing at elevated temperature. The photoelectrochemical and transient absorption spectroscopy results indicated that a short charge carrier lifetime limits the performance of Ni—Mo/NiFe$_2$O$_4$ photocathodes.

Introduction

Direct conversion of sunlight, CO$_2$, and H$_2$O into chemicals can be achieved in photoelectrochemical cells.[1–5] The functionality of such cells depends on photoelectrodes containing semiconductors, which absorb light and generate electrons and holes with sufficient potential to drive conversion of (CO$_2$ and) H$_2$O into fuel-type molecules such as methane, methanol, and hydrogen.[6] Stability of photoelectrodes is improved by deposition of a metal layer, which protects the semiconductor against photocorrosion.[7]

Performance is largely determined by the quality of the metal–semiconductor interfaces. Methods such as physical vapor deposition (PVD) or chemical vapor deposition (CVD) are often utilized to achieve optimized interfaces.[8,9] However, these processes are quite expensive and require specialized equipment. An all-wet electrochemical process would be more desirable.[8] An example of an electrochemical method for the formation of metals on semiconductors is galvanic displacement.[8,10,11] This is a so-called electroless deposition method, which does not require an external bias to drive electrochemi-

cal reactions. During galvanic displacement, the surface of the semiconductor in contact with the metal–cation solution is oxidized while the metal layer is simultaneously formed by reduction of the cations. The method is suitable for functionalization of, for example, Si or Ge surfaces,[8] after pretreatment with hydrogen fluoride-based solutions to remove the native oxide. Unfortunately, galvanic displacement is typically unsuitable for formation of metal–metal oxide interfaces.[8,10]

Electrodeposition, whereby a potential is applied to drive redox reactions on electrodes, is a suitable alternative for galvanic displacement.[8,12–16] Anodic electrodeposition on semiconductors is already well-established, creating oxide layers on top of a semiconductor.[17,18] For a metal layer to be formed, cathodic electrodeposition is required. One of the big issues with cathodic electrodeposition on many metal oxide semiconductors is reduction of the metal oxide layer.[8]

To circumvent this issue, ion-exchange and electroless deposition are applied prior to electrodeposition. For example, Sn^{2+} ions have been adsorbed on a semiconductor–oxide surface. The material with adsorbed Sn^{2+} is immersed in a solution containing, for example, Ag$^+$ or Pd^{2+} cations, which react with the adsorbed Sn^{2+} to form Sn^{4+} and metallic Ag or Pd. This metallic layer then protects the semiconductor metal oxide during sequential electrodeposition. Pre-metallization can also be done by using the aforementioned PVD or CVD techniques.[8]

In this study, we investigated the possibility to directly deposit metal layers onto the metal oxide semiconductor NiFe$_2$O$_4$, which shows promising behavior when used as a photocathode.[19–24] This material can be metallized with Ni—

[a] J. H. J. Wijten, Prof. Dr. B. M. Weckhuysen
Inorganic Chemistry and Catalysis group
Debye Institute for Nanomaterials Science, Utrecht University
Universiteitsweg 99, 3584 CG Utrecht (The Netherlands)
E-mail: b.m.weckhuysen@uu.nl

[b] R. P. H. Jong, Prof. Dr. G. Mul
Photocatalytic Synthesis, MESA+ Institute for Nanotechnology
University of Twente, Meander 225, 7500 AE Enschede (The Netherlands)

Supporting Information and the ORCID identification number(s) for the author(s) of this article can be found under https://doi.org/10.1002/cssc.201800112.

Mo,[13,16,25,26] by making use of simple aqueous cathodic electrodeposition baths containing the metal precursors, sodium citrate as a complexing agent, and sodium hydroxide or ammonia to adjust the pH.[12,14,15,27] UV/Vis spectroscopy, X-ray diffraction (XRD), and focused ion beam scanning electron microscopy with energy dispersive X-ray spectroscopy (FIB-SEM-EDX) were used to demonstrate the feasibility of this simple, one-step metallization of $NiFe_2O_4$ through electrodeposition, resulting in novel Ni—Mo/$NiFe_2O_4$ photocathodes with a $NiFe_2O_4$ photoabsorbing layer and a stabilizing and catalytic Ni—Mo layer.

Results and Discussion

To ensure optimal oxidation of the layers, $NiFe_2O_4$ was formed by spin coating in a layer-by-layer fashion. During spin coating, a thin layer of precursor nitrates is formed. The formation of the spinel phase by decomposition of the nitrates requires effective access to oxygen. Furthermore, nitrogen should be able to exit the precursor layers. The growth of the $NiFe_2O_4$ layer on F:SnO_2/glass substrates is illustrated in Figure 1. Separate samples were synthesized and, on increasing the number of deposition cycles, the samples become increasingly more orange (Figure 1 A). SEM images of the cross sections made with FIB cutting (Figure 1 B) show that the thickness of the $NiFe_2O_4$ layer increases with the number of subsequent deposition

cycles and that the surface of the layers is rather smooth. The Pt layer was deposited on top of the semiconductor layer prior to FIB cutting to prevent damage to the underlying layers. Porosity between the F:SnO_2 and $NiFe_2O_4$, and between separate $NiFe_2O_4$ layers, can sometimes be observed, owing to initial roughness and suboptimal wetting of the previous layer, but is found sparingly when the F:SnO_2 layer is rougher. The chemical identity of each of these layers is confirmed, including the underlying conductive substrate layer. By cross-section EDX mapping (see the Supporting Information, Figure S1), the Fe/Ni ratio in the $NiFe_2O_4$ layer was found to be 1.9:1.

XRD analysis (Figure 1 C) confirmed the growth of the trevorite (spinel) $NiFe_2O_4$ phase, since with increasing thickness the related diffraction lines become more pronounced. UV/Vis spectroscopy (Figure 1 D) further confirmed the formation of the desired spinel phase. The band gap for $NiFe_2O_4$ is often reported to be 1.56 eV (795 nm); however, as can be seen in the UV/Vis spectrum, this is a low-intensity band, related to an indirect band gap between minority states.[28,29] More significant for light absorption is the band starting at 2.1 eV (600 nm), which is the transition between majority states, constituting a direct band gap. The valence band maximum (VBM) is located mainly on Ni and O. The conduction band minimum is mainly positioned on Fe and O. Due to Fe being in both octahedral and tetrahedral positions, there are two distinct gaps.[28,29] Finally, the band gap of the minority states is found to redshift with increasing thickness and to decrease in intensity. The redshift is explained by an increasing amount of Ni^{2+} ions occupying tetrahedral sites instead of the normal octahedral sites in the inverse spinel structures. This is possible owing to partial inversion of the spinel structures, whereas in the normal spinel the bivalent ions are in the tetrahedral position.[30,31] In Figure 1 E, the increase in thickness is plotted against the number of deposition cycles, showing linear growth of thickness with a rate of 40 nm/cycle.

A Ni—Mo layer was electrodeposited on $NiFe_2O_4$ to act as both a protective and a catalyst layer for the hydrogen evolution reaction (HER; Figure 2 A). The composition of the Ni—Mo layer was found to be 77.3% Ni and 22.7% Mo by inductively coupled plasma atomic emission spectroscopy (ICP-AES).

The faradaic efficiency of electrodeposition was found to be 7.5% in Ni and 6.6% in Mo. This low current efficiency can be explained by the fact that the material formed is a hydrogen evolution catalyst and that the deposition is carried out at potentials allowing hydrogen evolution. A significant portion of the current is thus invested in hydrogen evolution. Mild pH values and an intermediate deposition current were chosen to stabilize the $NiFe_2O_4$ layer. Insufficient currents result in too much exposure to the deposition bath (considering the required deposition time), damaging the oxide layer, whereas excessive currents cause reduction of the oxides.
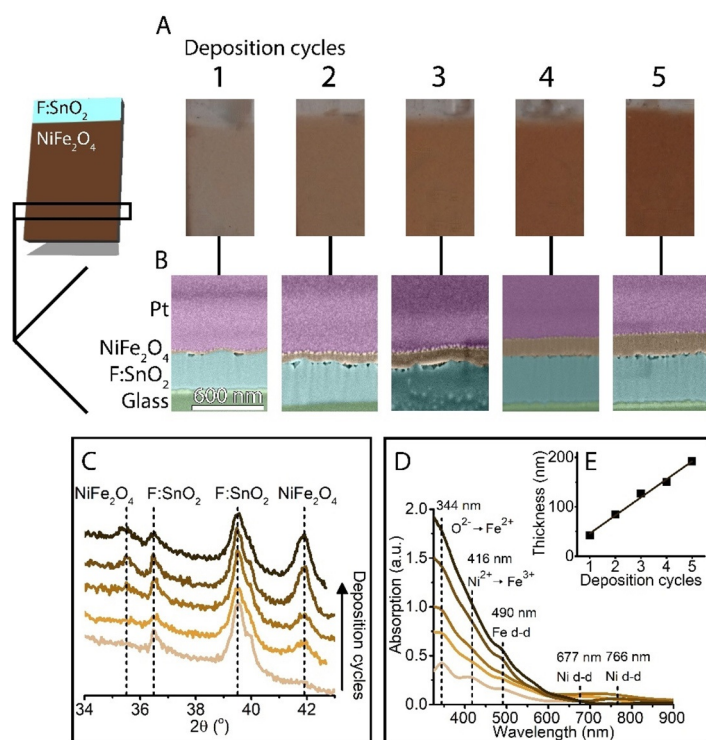

Figure 1. A) From left to right: a schematic representation of the $NiFe_2O_4$ film coated on F:SnO_2/Glass substrates followed by photographs of samples with 1, 2, 3, 4, and 5 layers of spin-coated $NiFe_2O_4$. B) SEM cross section images of (from left to right) 1, 2, 3, 4, and 5 deposition cycles of $NiFe_2O_4$. The various layers have been coloured: Pt = pink; NiFe_2O_4 = orange; F:SnO_2 = cyan; glass = green. C) XRD of the spin-coated $NiFe_2O_4$ layers with increasing thickness. D) UV/Vis spectra of the spin-coated $NiFe_2O_4$ samples. E) The increase in thickness with increasing deposition cycles.
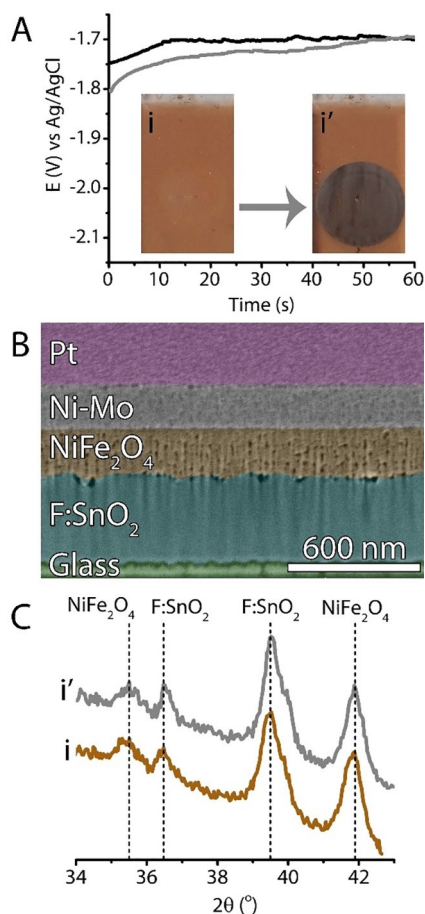
Figure 2. A) Ni–Mo electrodeposition (at −20 mA) curves on bare F:SnO₂/glass (black) and on NiFe₂O₄/F:SnO₂/glass with 5 spin-coating cycles (gray). Photographs show the NiFe₂O₄ sample before (i) and after (i') Ni–Mo electrodeposition. B) SEM cross-section image of the Ni–Mo/NiFe₂O₄/F:SnO₂/glass sample. The various layers have been colored: Pt = pink; NiFe₂O₄ = orange; F:SnO₂ = cyan; glass = green. C) XRD of NiFe₂O₄ with 5 spin-coating cycles before (i, orange) and after (i', gray) Ni–Mo electrodeposition.

However, we found that NiFe₂O₄ can be metallized without deterioration of the oxide layer (Figure 2). This means that the stability of the spinel structure against reduction is sufficient during electrodeposition at the applied current. Electrodeposition curves for bare F:SnO₂ and on NiFe₂O₄ are shown in Figure 2A, indicating little variation in the curves. Slightly higher potentials are required for the deposition of Ni–Mo on NiFe₂O₄, which is ascribed to the additional resistance introduced by NiFe₂O₄ to the entire system, which is 21–30 Ω for the NiFe₂O₄ layers on fluorine-doped tin oxide (FTO) compared to 12–15 Ω for bare FTO glass. The cross section (Figure 2B) shows a homogeneous layer of Ni–Mo has indeed formed of about 200 nm in thickness. The NiFe₂O₄ is also still 200 nm thick.

The apparent increase in porosity in the NiFe₂O₄ is not a result of the electrodeposition, but rather due to inhomogeneities in the film structure of NiFe₂O₄ after spin-coating (Figure S2). XRD analysis confirmed that the electrodeposition process did not affect the crystallinity of the spinel structure. Electrodeposition was successful for all thicknesses of the NiFe₂O₄

films. UV/Vis spectroscopy data could not be reproduced, owing to the reflective metal layer. The synthesis technique can also be extended to other metal coatings (Cu, Co–Mo; Figure S3), indicating that electrodeposition is a rather versatile method for functionalization of NiFe₂O₄.

To test the catalytic activity and stability towards the HER, the samples were suspended in 1 M KOH and cyclic voltammetry (CV) was measured in absence and presence of illumination (Figure 3A). Two reversible electrochemical peaks are observed
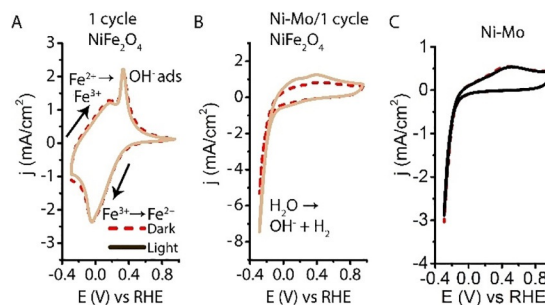

Figure 3. A) Cyclic voltammograms of 1 layer thick NiFe₂O₄. The dashed red lines show the dark current after 10 cycles in the dark. The solid lines show the light current after 10 cycles in the light. The cycles in the light were performed after the cycles in the dark. B) Cyclic voltammogram of Ni–Mo electrodeposited on 1 layer of NiFe₂O₄. C) Cyclic voltammogram of Ni–Mo electrodeposited directly on bare F:SnO₂/glass.

for a single layer of NiFe₂O₄. Firstly, at −0.02 V a reductive peak is observed, which is explained by reduction of Fe³⁺ to Fe²⁺. When sweeping towards the oxidative side, the oxidation of Fe²⁺ to Fe³⁺ is first observed at approximately 0.15 V. A sharper irreversible peak is then observed at 0.34 V, which is typical for hydroxide adsorption.[32] Since the CVs for bare NiFe₂O₄ are identical in the absence and presence of illumination, reduction of NiFe₂O₄ is the main contribution to the observed current within this timescale.

The combined Ni–Mo/NiFe₂O₄ system (Figure 3B) is quite different in its redox chemistry and photoresponse compared to bare NiFe₂O₄. In the dark cycle, the Fe reduction and Fe oxidation peaks are absent. Furthermore, the hydroxide adsorption peak is more broadened than that for pure NiFe₂O₄. Also notable is the increase in hydrogen evolution current, indicating a reduction in overpotential for the formation of hydrogen. Finally, for the combined system, a distinct photocurrent is detected, reaching −2.1 mA cm⁻² at −0.3 V. Clearly, the Ni–Mo layer largely protects the NiFe₂O₄ layer against oxidation/reduction cycles and shows a strong positive effect with regard to the photoresponse. The CV of Ni–Mo deposited directly on F:SnO₂ (Figure 3C) shows a small, broad hydroxide adsorption peak, while, as expected, the material shows neither the Fe redox couple nor a photoresponse.

To explore the stability of the samples over time, chronoamperometry was performed first for 5 min in the dark (Figure 4), and then for 1 h cycling of light on/off every 5 min (Figure 5). In the first 100 s the samples without Ni–Mo behave similarly (Figure 4). A strong increase in reductive current and a delay in active gas production (saw-tooth pattern) are observed during
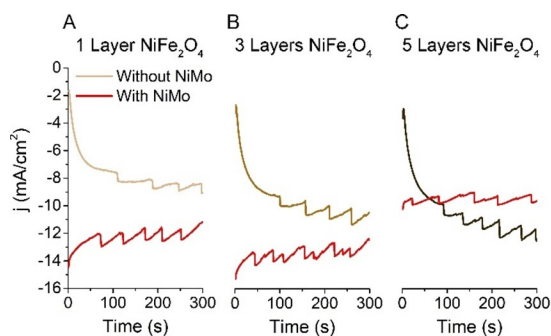
Figure 4. A) Chronoamperometry for 5 min on 1 layer thick $NiFe_2O_4$ samples without (brown) and with (red) Ni—Mo at a constant potential of -0.3 V vs. RHE in the dark, prior to the 1 h long measurement (Figure 5). B) Chronoamperometry on 3 layer thick $NiFe_2O_4$ samples. C) Chronoamperometry on 5 layer thick $NiFe_2O_4$ samples.

this period. This is due to the initial reduction of the exposed $NiFe_2O_4$ surface, after which hydrogen starts to evolve from the reduced electrode. In contrast, a slight decrease in current is observed for the Ni—Mo coated samples in the first 5 min. This is attributed to the HER, which introduces mass transport limitations on and near the electrode surface in the form of hydrogen gas bubbles.

The 1 hour chronoamperometry experiments are shown in Figure 5. Clear photocurrents are observed for several samples. The apparent increase in current seen for bare $NiFe_2O_4$, as a function of increasing layer thickness, is explained by an increased microporosity, as seen in SEM, and thus an increase of the electrochemical surface area. Furthermore, the samples of larger thicknesses (5 layers) do not show any significant photocurrent (black curve). This suggests that the top layers of $NiFe_2O_4$ are reduced at the applied potential, limiting photoactivity. After the chronoamperometric measurements, ICP-AES was performed on the electrolyte, showing that Ni leaches into the electrolyte in the absence of a Ni—Mo catalyst layer (Table S4).

All samples with the Ni—Mo catalyst layer showed comparable currents (Figure 5). The small variation is ascribed to differences in the electrochemical surface areas of the samples. The

highest photocurrent is reached for the thinnest sample, which is -2.1 mA cm^{-2} at -0.3 V, similar to the observed photocurrent in Figure 3. With increasing thickness of $NiFe_2O_4$, the photocurrent decreases. This suggests that charge carrier dynamics are a limiting factor.

Assuming that the diffusion length of charge carriers is comparable between samples, recombination of the photogenerated charges becomes more prevalent as the distance to be traveled increases. Furthermore, since samples are illuminated from the back and the amount of photogenerated charges is directly related to the light intensity, it follows that the relative amount of charge carriers is less close to the electrochemical interface for a thicker $NiFe_2O_4$ layer. Thus the addition of light absorber layers effectively lowers the photoresponse for these photoelectrodes.[32] Finally, incident photon to current efficiencies (IPCE) were determined at 420 nm (Figure S5).

Degradation of bare $NiFe_2O_4$ during the photoelectrochemical tests can be seen by eye (Figure 6A and Figure S6). The $NiFe_2O_4$ samples show a lighter, grayish circle where the material was exposed to the electrolyte during photoelectrochemistry (PEC), which is not observed for the Ni—Mo coated samples. This loss of absorber material is further supported by UV/Vis spectroscopy measurements (Figure 6B). When comparing the samples from before and after the catalytic tests, the absorption of each material is lower after the test. Finally, it can be observed by XRD (Figure 6C) that the $NiFe_2O_4$ diffraction lines of bare $NiFe_2O_4$ were slightly decreased after PEC. On the other hand, the Ni—Mo/$NiFe_2O_4$ photocathode retained its crystallinity.

Thus, we find that bare $NiFe_2O_4$ is an unstable material for light-driven hydrogen evolution from water splitting in alkaline conditions. Coating with Ni—Mo, however, stabilizes the system and furthermore improves the activity of the photoelectrode, if the $NiFe_2O_4$ is of limited thickness. A possible explanation for the instability under illumination is limited charge carrier mobility, making the material more prone to corrosion, as supported by the observation that Ni leaches into solution if the Ni—Mo layer is absent.

To explore the charge carrier dynamics of the $NiFe_2O_4$ samples in more detail, we used transient absorption spectroscopy
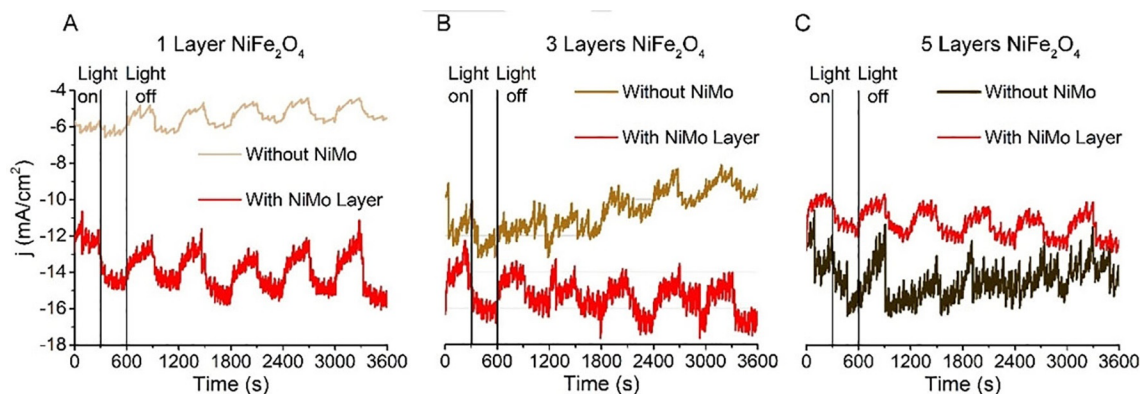

Figure 5. A) Chronoamperometry for 1 h on 1 layer thick $NiFe_2O_4$ samples without (brown) and with (red) Ni—Mo at a constant potential of -0.3 V vs. RHE while cycling light on and off every 300 s. B) Chronoamperometry on 3 layer thick $NiFe_2O_4$ samples. C) Chronoamperometry on 5 layer thick $NiFe_2O_4$ samples.
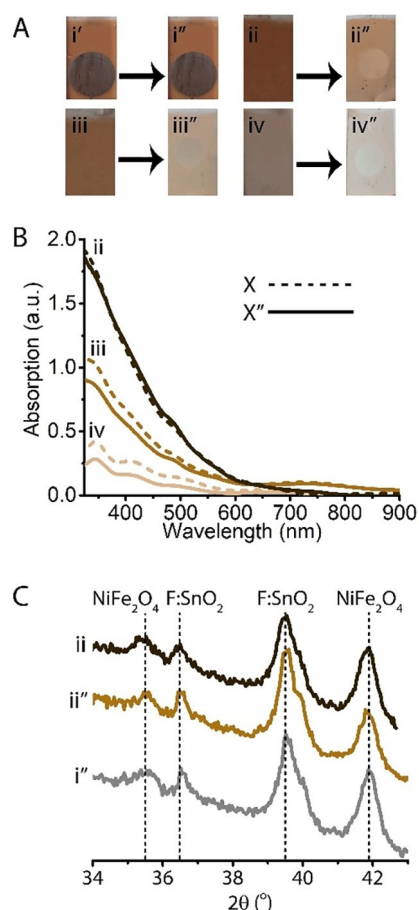
Figure 6. A) Photographs of fresh samples and spent samples (indicated by " for samples after conducting the PEC experiments). Ni–Mo/NiFe₂O₄ (i'), and NiFe₂O₄ with 5 (ii), 3 (iii), and 1 (iv) spin-coating cycles are shown. The color difference between the bulk of each photograph is due to different incident light from the surroundings when the pictures were taken. B) UV/Vis spectra of the NiFe₂O₄ samples before (dashed) and after (solid) photoelectrochemical tests. C) XRD of fresh 5 cycle NiFe₂O₄ (ii), spent 5 cycle NiFe₂O₄ (ii''), and spent Ni–Mo/NiFe₂O₄ (i'').

(TAS). The results are given in Figure 7, where the data are given for samples without Ni–Mo coating, and were measured in transmission mode. Only lifetimes and relative peak intensities can be compared. TAS data for samples including the Ni–
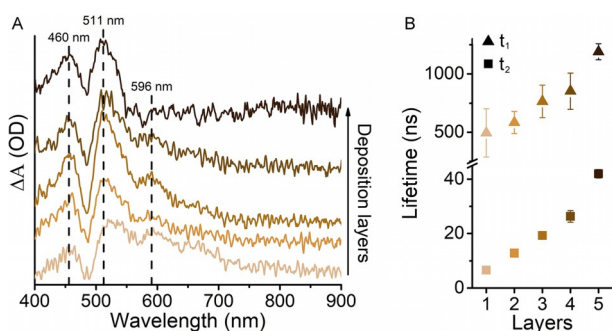

Figure 7. A) TAS spectra of fresh bare NiFe₂O₄ samples with increasing layer thickness, collected in transmission mode at a decay time of 1 ns. B) Averaged lifetimes obtained for the kinetic traces.

Mo layer are shown in in the Supporting Information (Figure S7).

Several transient signals are observed for each sample, each having similar decay times per sample, after pumping with 355 nm light (thus the $O^{2-} \rightarrow Fe^{2+}$ transition). The reader is kindly referred to the Supporting Information, Section S8, for the exact fitting results. In the kinetic traces the most intense signal around 511 nm (Figure 7), a slight shift in the maximized wavelength was found, which indicates that the electronic structure is slightly different for each material.

Transient absorption is observed at 511 nm, but also at 460 and 596 nm (Figure 7A). Two decay components are found, with a short (t_1, 2–50 ns) and a longer lifetime (t_2, 500–1100 ns). Most notably, both the short (t_1) and the long (t_2) lifetime-type transients increase as a function of NiFe₂O₄ layer thickness (Figure 7B). Since these measurements are performed ex situ in air, the dominant decay pathway in bare NiFe₂O₄ samples is via recombination of charges. The short lifetimes of charge carriers indicate slow diffusion and high likely hood of recombination. However, in the samples with a thicker NiFe₂O₄ layer the crystallinity is improved for the earlier deposited layers, through exposure to multiple heating steps. The increased crystallinity results in a material with fewer defect sites, thus extending the lifetime of the photogenerated charges.[33,34] Although at first glance the increased lifetime of the probed states seems to contradict the PEC results (Figure 5), it is important to point out that the entire light absorber layer is probed. This entails that even though on average the lifetime of photogenerated states has increased, this increase is mainly due to the enhanced performance of the layers underneath the last spin coated NiFe₂O₄ layer.

As reported by Meinert and Reiss[28] it is not straightforward to describe complex band structures, such as that of NiFe₂O₄. Nevertheless, based on our UV/Vis and TAS data as well as the results of Meinert,[28] we have derived a schematic representation of the electronic behavior of NiFe₂O₄ (Figure 8). First of all, excitation by 355 nm laser pump light excites electrons from
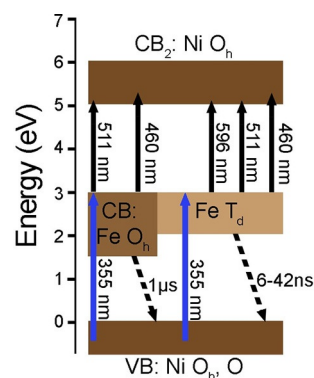

Figure 8. Schematic representation of the electronic structure of NiFe₂O₄. The valence band is positioned at 0 eV on the Ni^{2+} and O^{2-} species. The conduction band contains both O_h $Fe^{2+/3+}$ minority species and T_d Fe^{3+} majority species. Finally, the higher positioned conduction band is again Ni^{2+}. Light transitions of 355 nm as pump light (blue arrows) and 460, 511, and 596 nm are shown as probe light (black arrows). Several decay pathways of charge carriers are shown with the relevant lifetimes (dashed arrows).

the valence band (VB), positioned on Ni O_h and O, to the conduction bands positioned on both O_h (minority) and T_d (majority) Fe. From the O_h Fe species, transitions of 511 nm (2.43 eV) and 460 nm (2.69 eV) are possible. The O_h Fe species relax back to the VB following a slow decay (t_2) in the order of 1 μs. This decay is slow because this is a transition between minority states, also observable from the fact that ΔA is 5–10 times smaller for this t_2 component than it is for t_1. From the T_d Fe species, transitions of 511, 460, and 596 nm (2.08 eV) are possible. The T_d Fe species decays much faster, according to t_1 in the order of 10 ns, because here majority states are considered. The energy scales of the observed optical transitions agree with the described density of states reported by Meinert and Reiss.[28]

Although this strongly indicates that the assignment of transitions is correct, it is not possible from this data to be conclusive about the exact origins of the decay components. To ascertain this, more experiments, such as transient X-ray absorption spectroscopy, would be required to observe the electronic states. This is, however, outside the scope of this work and will be the subject of a separate work. To summarize, the data obtained indicate that charge carrier dynamics are observable on ns timescales, which suggests fast recombination and a short diffusion length. This is in agreement with the photoelectrochemical measurements and explains why a bias is necessary to observe any significant photocurrent.

Conclusions

$NiFe_2O_4$ can be formed homogeneously by spin coating on FTO-functionalized glass substrates. Thickness control down to 40 nm was achieved. Cathodic electrodeposition was successfully applied to deposit a film of Ni—Mo on top of $NiFe_2O_4$. The $NiFe_2O_4$ semiconducting layers were found to be stable during the synthesis process. Bare $NiFe_2O_4$, nor Ni—Mo showed photoactivity for hydrogen evolution. However, the studied Ni—Mo/$NiFe_2O_4$ photocathodes clearly performed better, and photocurrents up to -2.1 mA cm^{-2} were observed at -0.3 V vs. RHE, showing strong synergistic effects. We found that thinner light-absorbing layers yielded the highest photocurrents. This is ascribed to the photoinduced charge carrier diffusion length being a limiting factor for $NiFe_2O_4$. This observation is complemented by the TAS experiments, which indicate the photogenerated charge lifetimes to be on the order of ns. During continuous operation at -0.3 V vs. RHE under cycled light, we found that without Ni—Mo layers the samples are unstable, whereas with Ni—Mo the material is stabilized over the course of at least 1 h. The instability during photoelectrochemistry was found to be related to Fe and Ni reduction and oxidation. In summary, new semiconductor–metal constructs can be formed by a facile electrodeposition process without reduction of the semiconductor phase, enhancing the performance of $NiFe_2O_4$ in cathodic photoelectrochemical hydrogen production, both in terms of stability and activity.

Experimental Section

Materials

All materials were used as received without further purification. $NiSO_4 \cdot 6 H_2O$ (ReagentPlus, >99% pure), $NaMoO_4 \cdot 2 H_2O$ (ACS reagent, >99% pure), NaOH (99.99% trace metals, semiconductor grade), KOH (ACS reagent, >85% pure), $Na_3C_6H_5O_7 \cdot 2 H_2O$ (sodium citrate, ACS reagent, >99% pure), and $Fe(NO_3)_3 \cdot 9 H_2O$ (ACS reagent, >98% pure) were obtained from Sigma Aldrich. $Ni(NO_3)_2 \cdot 6 H_2O$ (99%), citric acid (RNase/protease free, anhydrous), and ethanol (anhydrous, extra dry, 99.5%) were obtained from Acros. Ethylene glycol (P.a. reag., Ph. Eur. >99.5%) was obtained from Fluka. NH_3 28–30% (ACS reagent, ph. Eur. for analysis) was obtained from Emsure. Fluorine-doped tin oxide glass (FTO, grade TEC 15) was obtained from Pilkington.

Spin coating of $NiFe_2O_4$

3×3 cm^2 F:SnO$_2$ coated glass slides were cleaned by first washing them with detergent (Eurobac hygienic soap 406 307) followed by subsequently sonicating them for 15 min in a 1:1:1 mixture of acetone, ethanol, and demineralized water, then in a 1 M HCl solution, and finally in demineralized water. As a last step, the slides were treated in a UV ozone cleaner for 15 min. $Fe(NO_3)_3$ (2 mmol), $Ni(NO_3)_2$ (1 mmol), and citric acid (3 mmol), were dissolved in anhydrous ethanol (10 mL). This solution was stirred for at least 2 h. Ethylene glycol (0.2 mL) was then added and the solution was stirred overnight. Prior to spin coating, the solution was filtered and a 300 μL sample was dropped onto the FTO slides. This was then spun at 3000 rpm for 60 s on an Electronic Microsystems Ltd. Model 4000 photoresist spinner. Part of the resulting thin layer of solution was removed by using an ethanol-wetted cotton tip to keep a part of the FTO slide free for electrical connections. It was then dried under ambient conditions for about 10 min, then heated on a hotplate at 100 °C for 10 min and finally heated to 450 °C for 30 min. This spin coating–oxidation procedure is referred to as one cycle.

Metallization of the metal oxide layers

The $NiFe_2O_4$ samples were fixed in a custom-made cell, as shown in Figure S9, for electrodeposition. Note that the FTO slides obtained through spin coating had to be cut into 3×1.5 cm^2 pieces before performing electrodeposition. Electrodeposition was performed galvanostatically at a current of -20 mA for 60 s. A Pt mesh (Mateck, 99.9%+) was used as a counter electrode and 3 M Ag/AgCl (BASi) was used as a reference electrode. The plating bath contained 0.3 M $NiSO_4$, 0.2 M Na_2MoO_4, and 0.3 M $Na_3C_6H_5O_7$ in demineralized water (100 mL). To this, NH_3 solution (20 mL) was added to obtain a pH of 9.2. First the metals were dissolved in water through stirring, then NH_3 was added to adjust the pH. Prior to the syntheses, the baths were purged with Ar for 15 min, and a gentle Ar flow was kept over the solution during electrodeposition.

Measurements and characterization

X-ray diffraction (XRD) was measured by using a Bruker D2 Phaser instrument. Most scans were taken at $2\theta = 34$–43° with 0.02° steps at a rate of 10 s per step while rotating at 15 Hz. UV/Vis spectroscopy was performed by using a Varian Cary 50 spectrometer. The spectra were obtained in transmission mode, in the range of 300–

1000 nm using clean FTO as a reference. Inductively coupled plasma atomic emission spectroscopy (ICP-AES) was performed on an Optima 8300 instrument from PerkinElmer and an average of three samples was used. Electrodeposited samples were dissolved in 2% HNO_3 (10 mL) before oxidation. It was then diluted further by adding 2 mL of the reaction mixture sample to 8 mL of 2% HNO_3. Ni (231.604 and 341.476 nm), Fe (238.204 and 259.939 nm), Co (228.616 and 236.380 nm), Cu (327.393 and 324.752 nm) and Mo (202.031 and 204.597 nm) were then measured. Calibration curves of 0, 0.2, 0.4, 0.6, 0.8, and 1.0 mg L^{-1} were prepared of all the metals. Focused ion beam scanning electron microscopy with energy-dispersive X-ray spectroscopy (FIB-SEM-EDX) was performed on a FEI Helios nanolab 600 DualBeam with an Oxford Instruments Silicon Drift Detector X-Max energy-dispersive spectroscope. EDX mapping was performed with an electron beam of 5 kV and 0.2 nA. The beam used to obtain several images is described in the captions. All SEM imaging was done by using secondary electrons at 2 kV and 0.1 nA. FIB cuts for cross sectional images were made by covering an area of 5×2 μm^2 of the substrate with 500 nm of Pt by sputtering at 30 kV and 0.08 nA. Then a cut of 7×5 μm^2 and 5 μm deep was made with the ion beam at 30 kV and 2.5 nA. Finally, the cross section was cleaned with an ion beam at 30 kV and 0.23 nA in an area of 6×0.5 μm^2 and 5 μm deep near the edge. An image was then taken from the sample at a 52° tilt. Transient absorption spectroscopy (TAS) was performed on an EOS spectrophotometer. The pump laser was generated by using a Nd:YAG crystal (1064 nm light) and transformed into 355 nm by using harmonic crystals. This laser was operated at a repetition rate of 1 kHz and the intensity was kept at 1.5 mW by using a neutral density filter. The probe pulse was generated by using a Leukos supercontinuum light source generating a wide spectrum detected between 350 nm and 900 nm with a spectral resolution of 1.5 nm. The repetition rate of the source was 2 kHz. The pulse duration of the lasers was below 1.2 ns, allowing for a temporal resolution below 1 ns. The probe light was split by using a beam splitter into dual beam mode so that unfiltered light could be used to correct for fluctuations in the light source. The samples were measured in transmission mode and were probed for 1 h under ambient air conditions. The samples coated with Ni—Mo were measured in reflectance mode and were probed for 2 h under ambient air conditions.

Photoelectrochemical tests

Photoelectrochemical tests were performed in 1 M KOH purged with N$_2$ for at least 15 min. The samples are mounted against a window with a diameter of 6 mm, exposing 0.28 cm^2. The reference electrode is a Hg/HgO electrode (0.956 V vs. RHE at pH 14) and the counter electrode is a Pt mesh. Chronoamperometry measurements are performed at a potential of −0.3 V vs. RHE for 1 h where light is cycled between dark and light every 300 s, starting in the dark. Prior to these measurements each sample was subjected to 5 min of chronoamperometry in the dark at −0.3 V vs. RHE. During the cyclic voltammetry experiments the potential is cycled from 0.956 V to −0.294 V vs. RHE for 10 cycles at 100 mV s^{-1}. All these photoelectrochemical tests were performed on a VersaSTAT 4 potentiostat from Princeton Applied Research. Directly afterwards, 10 more cycles were performed while the sample was back-illuminated with a Newport AM 1.5 solar simulator (100 mW cm^{-2}) consisting of a 300 W Xe lamp filtered with an air mass 1.5G filter. Calibration was performed with a standard reference Si solar cell prior to the measurements. IPCE measurements were taken by using a 420 nm LED light (380–460 nm spread, 1.5 mW cm^{-2}) at 20 mm distance on Ni—Mo coated samples with

the VersaSTAT 4 potentiostat from Princeton Applied Research. Prior to the IPCE measurements, the first three measurements were done in the dark for 5 minutes each, then one measurement was done in the light for 5 min. Bubble formation resulted in the data being averaged over these 5 min intervals.

Conflict of interest

The authors declare no conflict of interest.

[1] F. Fresno, R. Portela, S. Suárez, J. M. Coronado, *J. Mater. Chem. A* **2014**, *2*, 2863–2888.

[2] M. G. Walter, E. L. Warren, J. R. McKone, S. W. Boettcher, Q. Mi, E. A. Santori, N. S. Lewis, *Chem. Rev.* **2010**, *110*, 6446–6473.

[3] Y. Horiuchi, T. Toyao, M. Takeuchi, M. Matsuoka, M. Anpo, *Phys. Chem. Chem. Phys.* **2013**, *15*, 13243–13253.

[4] A. B. Djurišić, Y. H. Leung, A. M. Ching Ng, *Mater. Horiz.* **2014**, *1*, 400–410.

[5] X. Lu, S. Xie, H. Yang, Y. Tong, H. Ji, *Chem. Soc. Rev.* **2014**, *43*, 7581–7593.

[6] A. A. Ismail, D. W. Bahnemann, *Sol. Energy Mater. Sol. Cells* **2014**, *128*, 85–101.

[7] D. Bae, B. Seger, P. C. K. Vesborg, O. Hansen, I. Chorkendorff, *Chem. Soc. Rev.* **2017**, *46*, 1933–1954.

[8] *Electrodeposition and Surface Finishing* (Ed.: S. S. Djokić), Springer, New York, **2014**.

[9] J. Zhao, X. Wang, Z. Xu, J. S. C. Loo, *J. Mater. Chem. A* **2014**, *2*, 15228–15233.

[10] C. Carraro, R. Maboudian, L. Magagnin, *Surf. Sci. Rep.* **2007**, *62*, 499–525.

[11] L. Magagnin, P. Cojocaru, F. Secundo in *Electroless Synthesis of Metallic Nanostructures for Biomedical Technologies* (Ed.: S. Djokić), Springer, New York, **2012**, pp. 73–99.

[12] U. Lačnjevac, B. M. Jović, V. D. Jović, *Electrochim. Acta* **2009**, *55*, 535–543.

[13] M. Manazoğlu, G. Hapci, O. Gokhan, *J. Mater. Eng. Perform.* **2016**, *25*, 130–137.

[14] A. Saba, E. Elsayed, M. Moharam, M. M. Rashad, *ISRN Nanotechnol.* **2012**, *2012*, 532168.

[15] S. D. Sartale, C. D. Lokhande, V. Ganesan, *Phys. Status Solidi* **2005**, *202*, 85–94.

[16] C. Xu, J. Zhou, M. Zeng, X. Fu, X. Liu, J. Li, *Int. J. Hydrogen Energy* **2016**, *41*, 13341–13349.

[17] D. K. Zhong, M. Cornuz, K. Sivula, M. Grätzel, D. R. Gamelin, *Energy Environ. Sci.* **2011**, *4*, 1759–1764.

[18] J. A. Seabold, K. S. Choi, *Chem. Mater.* **2011**, *23*, 1105–1112.

[19] P. S. Bassi, Gurudayal, L. H. Wong, J. Barber, *Phys. Chem. Chem. Phys.* **2014**, *16*, 11834–11842.

[20] M. S. Prévot, N. Guijarro, K. Sivula, *ChemSusChem* **2015**, *8*, 1359–1367.

[21] C. G. Read, Y. Park, K.-S. Choi, *J. Phys. Chem. Lett.* **2012**, *3*, 1872–1876.

[22] G. Rekhila, Y. Bessekhouad, M. Trari, *Int. J. Hydrogen Energy* **2013**, *38*, 6335–6343.

[23] M. Sun, Y. Chen, G. Tian, A. Wu, H. Yan, H. Fu, *Electrochim. Acta* **2016**, *190*, 186–192.

[24] J. L. Gunjakar, A. M. More, K. V. Gurav, C. D. Lokhande, *Appl. Surf. Sci.* **2008**, *254*, 5844–5848.

[25] C. C. L. McCrory, S. Jung, I. M. Ferrer, S. M. Chatman, J. C. Peters, T. F. Jaramillo, *J. Am. Chem. Soc.* **2015**, *137*, 4347–4357.

[26] C. Fan, *J. Electrochem. Soc.* **1994**, *141*, 382–387.

[27] U. Lačnjevac, B. M. Jović, V. M. Maksimović, V. D. Jović, *J. Appl. Electrochem.* **2010**, *40*, 701–708.

[28] M. Meinert, G. Reiss, *J. Phys. Condens. Matter* **2014**, *26*, 115503.

[29] R. G. Burns, *Mineralogical Applications of Crystal Field Theory*, Cambridge University Press, Cambridge, **1993**.

[30] D. Carta, M. F. Casula, A. Falqui, D. Loche, G. Mountjoy, C. Sangregorio, A. Corrias, *J. Phys. Chem. C* **2009**, *113*, 8606–8615.

[31] C. N. Chinnasamy, A. Narayanasamy, N. Ponpandian, K. Chattopadhyay, K. Shinoda, B. Jeyadevan, K. Tohji, K. Nakatsuka, T. Furubayashi, I. Nakatani, *Phys. Rev. B* **2001**, *63*, 184108.

[32] G. Hodes, P. V. Kamat, *J. Phys. Chem. Lett.* **2015**, *6*, 4090–4092.

[33] S. R. Pendlebury, M. Barroso, A. J. Cowan, K. Sivula, J. Tang, M. Grätzel, D. Klug, J. R. Durrant, *Chem. Commun.* **2011**, *47*, 716–718.

[34] M. Barroso, S. R. Pendlebury, A. J. Cowan, J. R. Durrant, *Chem. Sci.* **2013**, *4*, 2724–2734.